Journal Pre-proof

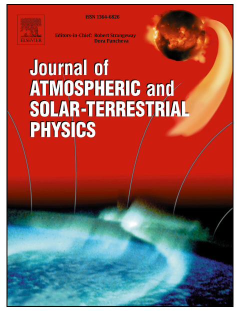

Duration and extent of solar X-ray flares and shortwave fadeouts likely to impact high frequency radio wave propagation based on an evaluation of absorption at 30 MHz

R.A.D. Fiori, N.C. Rogers, L. Nikitina, V. Lobzin, E. Rock

PII: S1364-6826(23)00146-3

DOI: https://doi.org/10.1016/j.jastp.2023.106148

Reference: ATP 106148

To appear in: *Journal of Atmospheric and Solar-Terrestrial Physics*

Received Date: 19 January 2023

Revised Date: 10 August 2023

Accepted Date: 30 September 2023

Please cite this article as: Fiori, R.A.D., Rogers, N.C., Nikitina, L., Lobzin, V., Rock, E., Duration and extent of solar X-ray flares and shortwave fadeouts likely to impact high frequency radio wave propagation based on an evaluation of absorption at 30 MHz, *Journal of Atmospheric and Solar-Terrestrial Physics* (2023), doi: https://doi.org/10.1016/j.jastp.2023.106148.

Duration and extent of solar X-ray flares and shortwave fadeouts likely to impact high frequency radio wave propagation based on an evaluation of absorption at 30 MHz

R. A. D. Fiori[1], N. C. Rogers[2], L. Nikitina[1], V. Lobzin[3], E. Rock[1]

[1]Canadian Hazards Information Service, Natural Resources Canada, Canada
[2]Space & Planetary Physics group, Department of Physics, Lancaster University, United Kingdom
[3]Science and Innovation Group, Bureau of Meteorology, Australia

Corresponding Author: Robyn Fiori
Telephone: 343-543-4006
email: robyn.fiori@nrcan-rncan.gc.ca

Keywords: shortwave fadeout, absorption, ionosphere, solar X-ray flare, space weather

Highlights:

- HF radio wave propagation at 5-15 MHz is impacted by ionospheric absorption when absorption at 30 MHz for a one-way vertical path is ≥ 0.5 dB.
- Expressions for the mean and 90th percentile duration were derived for solar X-ray flare events as a function of the peak 0.1-0.8 nm solar X-ray flux.
- The minimum solar X-ray flux expected to cause ionospheric absorption impacting HF radio waves is evaluated throughout the year for various latitudes.

Abstract:

High frequency (HF; 3-30 MHz) radio wave propagation can be impacted by absorption that results from enhanced photoionization in the dayside D-region following a solar X-ray flare. A database of > 25,000 solar X-ray flares was evaluated to characterize the relationship between flare duration and the peak of the 0.1-0.8 nm solar X-ray flux. Expressions describing the mean and 90th percentile duration were developed. Based on these models, mean durations of 13, 18, 27, and 39 minutes and 90th percentile durations of 30, 48, 77, and 123 minutes are expected for C1, M1, X1 and X10 solar X-ray flares, respectively. A probability distribution of flare durations was developed to describe the probability of flare duration lasting 0-15, 15-30, 30-45, 45-60, 60-90, >90 minutes. In addition to flare duration, the duration of the expected impact to HF radio waves was evaluated. By considering examples where HF radio wave propagation in the 5-15 MHz range was impacted by space weather, a 0.5 dB threshold at 30 MHz was observed in samples of riometer data. Absorption modelled at 1-minute increments from 1986-2017 was evaluated to create a probability distribution of impact duration, defined as the length of time the modelled 30 MHz absorption exceeded 0.5 dB during a single event. Modelled absorption was further evaluated to demonstrate the geographic extent of enhanced absorption, and to determine the minimum solar X-ray flux required to exceed the 0.5 dB impact threshold at a given latitude as a function of solar zenith angle and time of year. The results of this paper provide a better understanding of the impact of solar X-ray flares on high frequency radio wave propagation and aid in the development of tools and services for mitigating space weather impacts to systems that rely on HF radio wave propagation.

1. Introduction

Shortwave fadeout is a reduction of the strength (i.e. degradation) of high frequency (HF; 3-30 MHz) shortwave radio signals caused by increased photoionization on the Sun-facing side of the Earth following a solar X-ray flare (e.g., Mitra, 1974). Hard X-rays penetrate into the D-region ionosphere increasing photoionization and the D-region ionospheric electron density, which in turn increases ionospheric absorption of radio waves (e.g., Belrose and Cetiner, 1962). Absorption occurs when free electrons in the plasma that are impelled into motion by the radio wave lose their energy through collisions with ions and neutrals. The product of free electron density and electron collision frequency is highest at D-region altitudes (50-90km) and hence this is where most radio wave absorption occurs. The electron collision frequency in this region depends largely on the neutral particle density and temperature, which change relatively slowly. However, during solar flares, photoionization can increase the electron density significantly and on short timescales, leading to a near-instantaneous increase in HF radio wave absorption. Other phenomena that increase D-region electron density and therefore increase radio wave absorption, which are not considered in this paper, include collisional ionization by energetic auroral electrons, which cause Auroral Absorption, or solar energetic protons, which cause Polar Cap Absorption.

The magnitude of shortwave fadeout is related to solar flare magnitude. Solar flares are classified either based on the Hα or peak solar X-ray flux classification schemes (Cliver, 2001). In the Hα scheme, flares are classified by the flare size and a subjective descriptor of the flare brightness. The second classification scheme, which is applied in this paper, is based on the peak solar X-ray flux F_{MAX} measured in the 0.1-0.8 nm band. Flares are classified as A, B, C, M, and X on a logarithmic scale representing threshold intensities of 10^{-8}, 10^{-7}, 10^{-6}, 10^{-5}, and 10^{-4} $\mathrm{Wm^{-2}}$, respectively. Each classification has 9 subdivisions that range from 1 to 9. For example, an X1.3 solar X-ray flare has a maximum solar X-ray flux of 1.3 x 10^{-4} $\mathrm{Wm^{-2}}$. The X subdivisions can exceed 10 to describe flares >X10. For strong solar X-ray flares the D-region electron density can increase as much as a factor of ~10 (Davies, 1990).

Loss of these HF signals impacts users that rely on HF radio wave propagation for communication such as the aviation community, military, and emergency response (e.g. Boteler et al., 2018; Cannon et al., 2013; Hapgood et al., 2021; Knipp et al., 2021). Acknowledging the risk of the potential interruption of HF communications due to space weather, including the impacts of shortwave fadeout, the International Civil Aviation Organization (ICAO) initiated the development of a space weather advisory service and identified thresholds for moderate and severe levels of activity (ICAO 2018; 2019). Fiori et al. (2022b) examined the occurrence rate and duration of solar X-ray flare events with respect to ICAO thresholds of X1 and X10 flare classification used to define moderate and severe activity, respectively. From a data set comprising > 50,000 ≥ C-class solar X-ray flares they identified 420 moderate and 18 severe events. Events were found to be distributed unevenly throughout the solar cycle with 84% of events being observed during solar maximum compared to solar minimum. Events were also found to be unevenly distributed between solar cycles with 51% of events being observed in the more active solar cycle 22 compared to solar cycles 23 and 24. Solar X-ray flares with peaks exceeding the moderate (X1) threshold were found to have a mean event duration of 68 minutes. Those crossing the severe (X10) threshold were found to be >30 minutes, with a mean duration of 132 minutes. Durations reported in Fiori et al. (2022b) demonstrate a general trend of increasing duration with increasing flare size, but a precise relationship between duration and the magnitude of the peak solar X-ray flux (F_{MAX}) was not determined.

The impact of absorption has also been demonstrated on HF systems that include, for example, the Super Dual Auroral Radar Network (SuperDARN) (Berngardt et al., 2018; Chakraborty et al., 2018; 2019; Fiori et al., 2018; Hosokawa et al., 2000; Kikuchi et al., 1986; Watanabe and Nishitani, 2013), the Reverse Beacon

Network and Weak Signal Propagation Reporter Network (Frissell et al., 2014; 2019), and mid-latitude digisonde data (de Paula et al., 2022). Shortwave fadeout has also been observed in low and middle latitude ionosonde systems, characterized either generally as a radio blackout, or by solar zenith angle dependent deviations in the minimum reflection frequency (f_{min}) or the deviation in f_{min} from a background level (Sripathi et al., 2013; Nogueira et al., 2015; Barta et al., 2019; Tao et al., 2020).

It is a common theme in the literature, to report this general trend between increasing flare duration and increasing solar X-ray flux without being able to exactly quantify the relationship between duration and F_{MAX} due to the spread in the data. Overwhelming evidence, primarily based on comparing distributions of flare duration for varying magnitudes of the peak solar X-ray flux, or comparisons of yearly averages of flare duration and flare intensity, usually characterized by flare class only, demonstrates this trend (e.g., Temmer et al., 2001; Veronig et al., 2002; Joshi et al., 2010; Xiong et al., 2021). Temmer et al. (2001) further break duration into the component prior to and post peak and demonstrate that the identified trend is more pronounced for decay time than rise time. Xiong et al. (2021) evaluated flare duration by solar cycle and observed longer durations during more active solar cycles, a relationship tied to the observation of stronger flares during more active solar cycles. In contrast, Reep and Knizhnik (2019) compared flare duration, as defined by the full width half maximum of the solar X-ray flux enhancement, and concluded there was no relation between duration and F_{MAX}, which was found to be related to multiple flare properties, including temperature, emission measure, and energy. However, they did notice a “slight tendency” for larger flares to last longer.

Tao et al. (2020) evaluated the duration of shortwave fadeout in ionosonde data. They defined shortwave fadeout duration as the time where the deviation of f_{min} from a 27-day running median exceeded thresholds of either 2.5 MHz, 3.5 MHz, or a blackout was observed. For each threshold they observed a positive correlation between increasing peak solar X-ray flux and shortwave fadeout duration for events when the solar zenith angle of the stations was 0°-45° for durations ≤ 1.5 hours. For solar zenith angles of 0°-45°, flares > X1, and durations > 1.5 hours a clear relationship was not detected. A relationship between flare magnitude and flare duration was not observed for larger solar zenith angles, possible due to the reduction in events.

Although a precise relationship between flare duration, or in the case of Tao et al. (2020), shortwave fadeout duration, and F_{MAX} has not been definitively derived in the past, this paper takes a closer look at flare duration in the context of operational service development to better characterize the risk associated with a flare of known magnitude. Event duration takes on two meanings in the context of risk assessment. The first is the duration of the solar X-ray flux enhancement which is derived from the 0.1-0.8 nm solar X-ray flux directly. The second is the duration of the impact expected, described here based on the absorption expected for a 30 MHz signal at a given location. To describe absorption, the shortwave fadeout absorption model presented by Fiori et al. (2022a) is used.

Fiori et al. (2022a) developed a simple shortwave fadeout model based on measurements of 30 MHz cosmic noise absorption from the Natural Resources Canada (NRCan) riometer network (Danskin et al., 2008; Lam, 2011). They modelled the absorption (A_{30}) expected at 30 MHz for a one-way vertical path as a function of the magnitude of solar X-ray flux and solar zenith angle (SZA) as

$$A_{30} = 12080F\cos(\mathrm{SZA}) \quad (\mathrm{dB}), \tag{1}$$

where F is the 0.1-0.8 nm solar X-ray flux in units of Wm^{-2}, and SZA is the solar zenith angle at the location where the absorption is being evaluated. The SZA dependence indicates absorption enhancements are most strongly felt at equatorial latitudes near local noon and fall off toward the poles and toward the nightside. The model is limited to purely dayside absorption from overhead solar illumination and therefore limits SZA to being strictly ≤ 90°. Based on an analysis of both the 87 events used to derive their model, and an additional 19-event test data set, Fiori et al. (2022a) showed good performance of the model. Agreement was strongest if events were independently evaluated and the coefficient 12080 was optimized based on a regression fit to the measured absorption. Equation (1) is applied throughout this paper to model absorption. Other shortwave fadeout models are physics based, solving dispersion equations to evaluate enhanced ionization by solving radiative transport equations (Eccles et al., 2005; Levine et al., 2019; Chakraborty et al., 2021). Physics-based models can be more accurate, but they tend to have a longer run time than the model described by equation (1), making them more difficult to use in an operational setting.

The objective of this paper is to assess the effect of shortwave fadeout on HF radio wave propagation by evaluating the duration of enhanced solar X-ray flux and absorption and the spatial distribution of enhanced absorption based on the model described by equation (1) and an evaluation of past events.

2. Data

2.1 GOES solar X-ray flux and X-ray sensor reports

Solar X-ray flux was obtained from the National Oceanic and Atmospheric Administration (NOAA) and National Aeronautic and Space Administration (NASA) Geostationary Operational Environmental Satellite Network (GOES) X-Ray Sensor (XRS) instrument (Machol and Viereck, 2016). The data considered were 1-minute values from GOES satellites 6-15 spanning a 32-year period from 1986 to 2017. The XRS measures solar X-ray flux in two wavebands within the solar X-ray spectrum: soft X-rays (0.1-0.8 nm) and hard X-rays (0.05-0.4 nm). Only soft X-ray data were considered in this study, as they are a primary source of D-region photoionization (e.g., Schumer, 2009). Following Machol and Viereck (2016), the 0.1-0.8 nm solar X-ray flux was divided by 0.7 to correct a scaling factor erroneously applied to the GOES 8-15 satellite data and to properly scale GOES satellite 6-7 data.

In addition to solar X-ray flux measurements, a database of solar X-ray flare events from 1997-2017 was evaluated, ending 28 June 2017. Data were taken from the GOES X-ray sensor reports (https://www.ngdc.noaa.gov/stp/space-weather/solar-data/solar-features/solar-flares/x-rays/goes/xrs/), which contain information on flare size, timing of the start, peak, and end of the flare, solar coordinates of the eruption, and the satellite used to collect the information. We removed some events from the data which were corrupt or anomalous. Anomalies included events where the start and peak or start and end time of the flare were equal, or time was not reliably determined. Flare magnitude was divided by 0.7 to correct the data, as described above. The corrected flare magnitude calculated from the GOES X-ray sensor reports was compared to corrected GOES X-ray flux data to ensure the correction factors were applied appropriately.

The remaining event list was then filtered to remove overlapping flares where one flare started before the previous flare ended. A minimum flare spacing of 5 minutes was required. Finally, statistics in this study are limited to the 25,603 solar X-ray flares classified as ≥ C1 as reported in the GOES X-ray sensor reports. Flares classified as < C1 cannot be consistently monitored across the solar cycle, especially during periods of high solar activity where they are obscured by the high background solar X-ray flux (e.g., Cliver, 2001; Xiong et al., 2021). Flares were predominantly C-class (86.1%), with 12.9% of events M-class, and 0.1% of events X-class. A thorough discussion of the occurrence frequency of C, M, and X-class solar X-ray flares is provided by Fiori et al. (2022b). Flares in the GOES X-ray sensor reports follow solar cycle trends with flares occurring more frequently and reaching larger peaks during solar maximum, and during more active solar cycles.

Event start, peak, and end times reported in the GOES X-ray sensor reports were used to evaluate the duration of solar X-ray flares. Timing in these reports, described in Swalwell et al. (2018), was determined from the GOES 0.1-0.8 nm wavelength solar X-ray flux. The onset of a solar X-ray flare was identified as the start of an interval of four consecutive points, at 1-minute resolution, where the following conditions were met: (1) all four values exceeded a B1 threshold (1×10^{-7} Wm^{-2}), (2) all four values were strictly increasing, and (3) the fourth value was at least 1.4 times greater than the first value. Peak time coincides with the peak solar X-ray flux observed after onset. Event end is defined as the time where the solar X-ray flux reaches 50% of the peak flux, where peak flux is taken to be the maximum flux minus flux at onset.

It is worth noting that these durations are not used universally. For example, Swalwell et al. (2018) reports inconsistencies in the flare durations determined from the GOES X-ray sensor reports. They observed the mean duration of flares occurring in Solar Cycles 21 (1976-1986) and 22 (1986-1996) were ~2.5 times longer for X-class flares and ~1.7 times longer for M-class flares than those reported in solar Cycle 23 (1996-2008), and attributed the discrepancy to flare timings being determined based on optical flares (Hα) prior to 1997 and X-ray flares after 1997. This is why data in this study were limited to events occurring no earlier than 1997. To correct the timing discrepancy, Swalwell et al. (2018) proposed new definitions for the flare start and end: Flare start is defined by moving backwards in time from the maximum flux and locating where either the flux reaches 5% of the peak value, or the slope of the flux curve reached 5% of the peak slope, and end time is defined by moving forward in time from the maximum flux and determining when flux reached 50% of the peak values. The GOES X-ray sensor reports data were used to draw comparisons with previous studies which evaluated similar data sets (Temmer et al., 2001; Veronig et al., 2002; Xiong et al., 2021), and to make use of a wider range of flare intensities by including C-class events which were not evaluated by Swalwell et al. (2018).

2.2 NRCan's HF transmitter network

NRCan operates an HF transmission network (Cameron et al., 2021). This paper makes use of data from the network's HF receiver located in Alert, Nunavut, Canada (82.50° N, 62.35° W) that regularly receives signals from a transmitter in Ottawa, Ontario, Canada (45.42° N, 75.70° W). The transmitter transmits at six frequencies (5.4, 6.9, 8.1, 11.1, and 14.4 MHz) using a pre-determined schedule that prevents transmissions from overlapping with other operational transmitters within the network. Cameron et al. (2021) provides a thorough description of the transmitter network, and describes characteristics of radio wave propagation over Canada.

2.3 SuperDARN

Data from the Super Dual Auroral Radar Network (SuperDARN) were used to establish an absorption threshold above which impacts to HF systems are expected. SuperDARN is a global network of HF coherent scatter radars that continuously monitors the ionosphere by examining the echoes of transmitted signals scattered off ionospheric irregularities (Chisham et al., 2007; Greenwald et al., 1995;

Nishitani et al, 2019). Each radar operates in the 8-20 MHz frequency band in 16-24 beam positions separated by ~3.24° in 75-110 range gates 45 km in length, beginning at 180 km range from the radar.

2.4 Riometer data and absorption

Equation (1) was derived using data characterizing absorption at 30 MHz collected from the NRCan riometer array, as described by Fiori et al. (2022a). Riometers measure ionospheric opacity to cosmic radio noise, which is represented by signal voltage (e.g. Browne et al., 1995). Deviation of the observed voltage from the voltage expected on an ionospherically quiet day (e.g. quiet day curve) is expressed as absorption, measured in dB (NORSTAR, 2014).

The NRCan riometers characterize signal voltage and absorption at 30 MHz. Each instrument has a wide-beam antenna characterizing the ionosphere directly overhead within a ~100 km radius. Riometer data are collected at a 1-second resolution and downsampled to a 1-minute resolution.

3. Absorption thresholds corresponding to the degradation of HF radio wave propagation

Assessing the risk of shortwave fadeout to HF radio wave propagation requires the establishment of thresholds to indicate when signal degradation, which can range from partial to complete (i.e. radio blackout) signal loss, is likely. However, the level of absorption is dependent on radio frequency, f, and is often modelled by a power law, $A(f) = A(f_0)\,(f/f_0)^{-n}$ (e.g., Davies, 1990). In this paper, we determine a threshold value for absorption along a one-way vertical path at a reference frequency, f_0 = 30 MHz, A_{30}, for which transmissions in the ~5-15 MHz range are expected to be degraded. This frequency range is relevant for HF radio wave propagation used for HF communication for airlines. For example (ICAO, 2010) recommends frequencies of 3-6.6 MHz for propagation on the nightside of the Earth, and 9-11.3 MHz and even > 13 MHz for propagation on the dayside of the Earth and indicates 20 MHz is the upper limit to the maximum useable frequency in the South Pacific. This frequency range is also relevant to Arctic surveillance, as discussed by Thayaparan et al. (2022) in relation to the development of an over-the-horizon radar operating at 2-22 MHz. A one-way vertical path at 30 MHz was chosen to represent 30 MHz riometer data typically used both to measure absorption and for global models of shortwave fadeout.

The importance of selecting absorption thresholds appropriate to the operating frequency is illustrated by Fiori et al. (2018), who presented observations from NRCan's 30 MHz riometer network for a shortwave fadeout event on 11 March 2015 in association with an X2.1 solar X-ray flare. During the same event, SuperDARN, operating at ~11 MHz, observed a suppression in the radar echo occurrence rate followed by a blackout. SuperDARN observed this drop in echo occurrence prior to the observed riometer response. The offset in time is due to the difference in observing frequencies. Assuming an empirical $f^{-1.24}$ relationship between frequency and absorption (Schumer, 2009), since the riometers operate at a higher frequency than the SuperDARN radars, riometers will observe the absorption enhancement later as the initial enhancement is below their sensitivity threshold. Shortly after the riometers registered an absorption enhancement, the SuperDARN signals experienced radio blackout. The blackout began roughly 10 minutes following the flare onset and lasted 10-30 minutes followed by a 10-40 minute recovery.

By combining data about the space weather environment at the onset of radio blackout, and a model of shortwave fadeout at 30 MHz, impact thresholds to an 11 MHz signal can be derived. Table 1 shows the onset of total radio blackout ($T_{blackout}$) for the 11 March 2015 event described in Fiori et al. (2018), and the 0.1-0.8 nm solar X-ray flux at the corresponding time ($F_{blackout}$). Modelling absorption using equation (1), A_{30} was calculated at the time of the onset of radio blackout ($A_{30\ blackout}$). SZA, also reported in Fiori et al. (2018), was calculated at 16:10 UT based on both the average location of all beam / range-gate cells recording either ground-scattered or ionospheric-scattered SuperDARN echoes between 16:10 UT and 16:18 UT, and at the location of the radar station. Given the radio signal passes through the D-region ionosphere somewhere between the SuperDARN radar station and the average echo location these SZA represent minimum and maximum possible values and the calculated absorption therefore also represent minimum and maximum values. A_{30} calculated at the average echo location varies from 0.27 dB to 0.69 dB, with mean and median values of 0.51 dB and 0.57 dB, respectively. If the calculations are repeated using the SZA of the SuperDARN radar station, A_{30} ranges from 0.52 dB to 0.86 dB with mean and median values of 0.67 dB. For the purposes of the risk analysis performed in this paper, and erring on the side of caution, we therefore suggest 0.5 dB as the threshold at which degradation of HF radio wave propagation is expected. At A_{30}=0.5 dB, frequencies < 11 MHz are expected to experience blackouts and frequencies > 11 MHz are likely to show some degradation, although blackout is not necessarily expected.

The GOES solar X-ray flux was used to model absorption from equation (1) at the SZAs listed in Table 1 for the 11 March 2015 event. The time at which absorption exceeded 0.5 dB is listed in the final column of Table 1. Based on the model, degradation was not expected at the two stations at the highest SZA where absorption peaked at 0.43 dB and 0.45 dB. $A_{30} \geq 0.5$ dB was first observed at the 16:19 UT for SZA ≤ 72°, and then progressed to 16:20 at 77.5° and 16:22 UT at 82.3°. The onset of signal blackout was within 0-2 minutes of the blackout observed by SuperDARN implying the 0.5 dB threshold is a reasonable representation of expected signal degradation.

To demonstrate the relevance of an A_{30}=0.5 dB threshold for HF signal degradation in another high-latitude systems, consider data from the Ottawa – Alert link within NRCan's HF transmitter network. Shortwave fadeout events are short lived. To better evaluate signal degradation with respect to the absorption threshold, we instead present an example of polar cap absorption which is prolonged and observed over a comparatively longer timescale.

Table 1: Onset of total radio blackout ($T_{blackout}$) based on SuperDARN observations, 0.1-0.8 nm solar X-ray flux at $T_{blackout}$ ($F_{blackout}$), and A_{30} at $T_{blackout}$ ($A_{30\ blackout}$). Data are for SuperDARN radars on 11 March 2015 based on an analysis of ground-scattered echoes performed in Fiori et al. (2018). Stations are arranged in order of decreasing solar zenith angle (SZA) (echo) where SZA (echo) is calculated at 16:10 UT based on the average location of both ground-scattered and ionospheric-scattered echoes recorded between 16:10 UT and 16:18 UT. SZA (radar) is calculated at the location of the radar station. The final column is the time at which A_{30} modelled from equation (1) exceeded 0.5 dB at the corresponding SZA (echo).

SuperDARN radar	SZA (°) (echo)	SZA (°) (radar)	$T_{blackout}$ (UT) (SuperDARN)	$F_{blackout}$ (Wm^{-2})	A_{30} blackout (dB) (echo)	A_{30} blackout (dB) (radar)	$T_{blackout}$ (UT) (A_{30} > 0.5 dB)
Prince George	83.5	77.4	16:20	1.99E-04	0.27	0.52	-
Pykkvibaer	83.2	73.5	16:20	1.99E-04	0.28	0.68	-
Christmas Valley West	82.3	71.6	16:20	1.99E-04	0.32	0.76	16:22
Clyde River	77.5	74.4	16:21	2.19E-04	0.57	0.71	16:20
Saskatoon	72.0	68.2	16:19	1.54E-04	0.57	0.69	16:19
Stokkseyri	71.5	73.2	16:19	1.54E-04	0.59	0.54	16:19
Fort Hayes West	68.8	55.9	16:18	9.96E-05	0.44	0.67	16:19
Christmas Valley East	68.1	71.6	16:19	1.54E-04	0.69	0.59	16:19
Kapuskasing	64.8	56.5	16:18	9.96E-05	0.51	0.66	16:19
Blackstone	56.8	44.1	16:18	9.96E-05	0.66	0.86	16:19
Fort Hayes East	56.7	55.9	16:18	9.96E-05	0.66	0.67	16:19

Consider a prolonged polar cap absorption event that occurred in February and March of 2014, illustrated in Figure 1. During this event the >10 MeV solar proton flux was elevated above the 10 $cm^{-2}\ sr^{-1}\ s^{-1}$ threshold characterizing a Solar Energetic Particle event between 14:00 UT on 25 February 2014 and 00:50 UT on 03 March 2014, with a peak flux at 12:00 UT on 28 February 2014. At ~130 hours duration, this is a long duration event. The onset, peak, and end times are marked by vertical dashed lines in Figure 1. The upper panel shows the occurrence of HF signals at frequencies of 5.4, 6.9, 8.1, 10.4, 11.1, and 14.4 MHz along the Ottawa - Alert transmission path. Each dot indicates when the signal was received. Some diurnal variation in signal occurrence is expected. Rotation of the transmission path across the sunlit portion of the polar cap, where photoionization increases ionospheric electron density and subsequent recombination processes on the non-sunlit portion of the polar cap change the range of useable frequencies. As a result, lower frequencies tend to be absorbed during the day and higher frequencies are not supported during the night. This diurnal variation is clearly seen both before the event onset and after the event end. During the event there are large gaps in the occurrence, especially at low frequency.

To better quantify this behaviour the ratio of the occurrence observed in an hour to the occurrence expected to be observed in an hour, was determined (see middle panel of Figure 1). The method for calculating the expected occurrence in the absence of absorption is thoroughly described in Cameron et al. (2021). Their method uses a "quiet day" baseline determined from the 80th percentile of hourly HF occurrence for quiet days drawn from the 30 days surrounding a given time period. The proportion of zero points (0 signals received with >0 signals expected) during the event ranges from 71.4% at 14.4 MHz

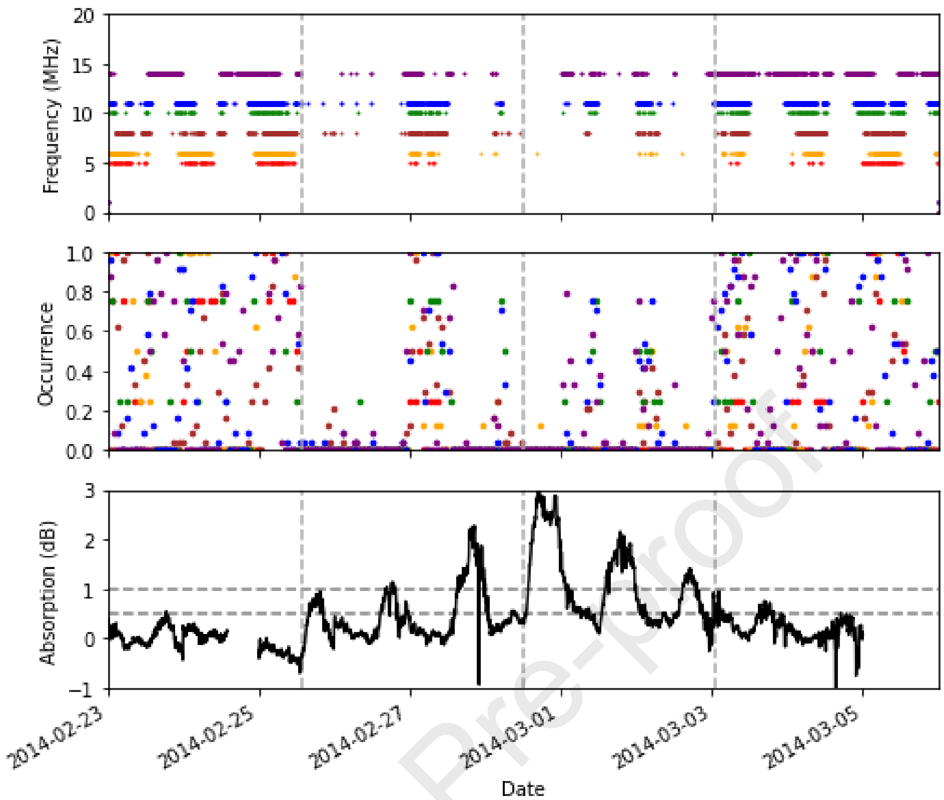

Figure 1: Data from the Ottawa - Alert radio wave propagation path 23 February - 05 March 2014 during a polar cap absorption event. From the top down, panels show (upper panel) periods of HF reception at each frequencies of 5.4, 6.9, 8.1, 10.4, 11.1, and 14.4 MHz, (middle panel) ratio of the number of signals observed in a 1-hour period to the number of signals expected in a 1-hour period where colour indicates frequency according to the upper panel, and (lower panel), absorption at 30 MHz observed at the Resolute Bay riometer station along the propagation path. Vertical lines in all plots indicate the onset, peak, and end of the solar energetic particle event. Horizontal lines in the lower panel indicate A_{30}=0.5 dB and A_{30}=1.0 dB absorption.

to 93.9% at 5.4 MHz compared to an average occurrence of 46.4% before and after the event. For this event, the expected diurnal variation in signal occurrence is enhanced when the transmission path is on the dayside and there is increased absorption. This is easily seen through comparison to data from a 30 MHz riometer located at Resolute Bay, Nunavut (74.7 N, 282.1 W) along the Ottawa - Alert transmission path. In the lower panel in Figure 1, riometer data indicate a pattern of enhanced absorption (at 30 MHz) when the station is located on the sunlit region of the polar cap, when the HF signals are degraded and blacked out, and reduced absorption on the nightside, when the HF signals return. During the dayside periods for the duration of the event, the absorption reaches or exceeds 0.5 dB absorption, and even reaches 3 dB at the event peak. Slight absorption enhancements of >0.5 dB persist after event termination and there are associated minor drops in the occurrence. This example demonstrates that A_{30}=0.5 dB is a relevant threshold that is indicative of degradation of 5.4-14.4 MHz signals and suggests 1 dB also be considered as an indicator of more severe signal degradation.

4. Evaluation of the duration and region impacted by shortwave fadeout

Forecasting the exact timing, magnitude and impact of a solar X-ray flare would be a powerful tool in a space weather forecaster's arsenal that is not yet within reach. Instead, risk mitigation, following a solar

X-ray flare must rely on an evaluation of event duration and probabilistic models of the region and extent of impact. Both are discussed in this Section in relation to the 0.5 dB threshold for A_{30} established in the previous section. In some cases, A_{30} is also evaluated against a 1.0 dB threshold to represent more severe signal degradation.

4.1 Duration of Solar X-ray flux events

The complete distribution of flare duration versus magnitude of the peak solar X-ray flux (F_{MAX}) provided by the GOES X-ray sensor reports is presented in Figure 2. Figure 2a is an occurrence density plot of flare duration, in minutes, against the logarithm of F_{MAX}. The data indicate a predominance of C-class flares lasting < 30 minutes. Longer flare durations are observed for the C-class flares, and shorter duration flares are observed for X-class flares, but the low occurrence of points for longer duration events and M and X class flares makes it difficult to observe any trends in the data. Presenting the data in a log-log form, Figure 2b, there is still a significant spread in the data and the Pearson Correlation coefficient is poor at only R=0.22. These results agree with Veronig et al. (2002) who present a similar log-log plot comparing flare duration and peak solar X-ray flux for events between 1976 and 2000, and found a weak correlation of R=0.25.

Table 2 indicates the minimum, maximum, mean and median flare duration for C, M, and X-class solar X-ray flares. Overall median duration is 14 minutes, which is 2 minutes longer than that reported by Veronig et al. (2002), and one minute less than values reported by Temmer et al. (2001) for a 1975-1999 data set, which was in agreement with the 12-15 minute durations separately reported by Xiong et al. (2021) for solar cycles 22, 23, and 24. Median flare duration increases with increasing flare magnitude; values of 13, 19, 26, and 36 minutes were determined for C, M, X1-X9, and ≥ X10 solar X-ray flares, respectively. Despite the observed trend of increasing median duration with increasing peak solar X-ray flux, the longest durations where observed for the lowest magnitude flares, with the longest duration event of 625 minutes being C-class whereas X-class flares had a smaller maximum duration of 188 minutes; a fact that might be attributed to the lower sampling of events.

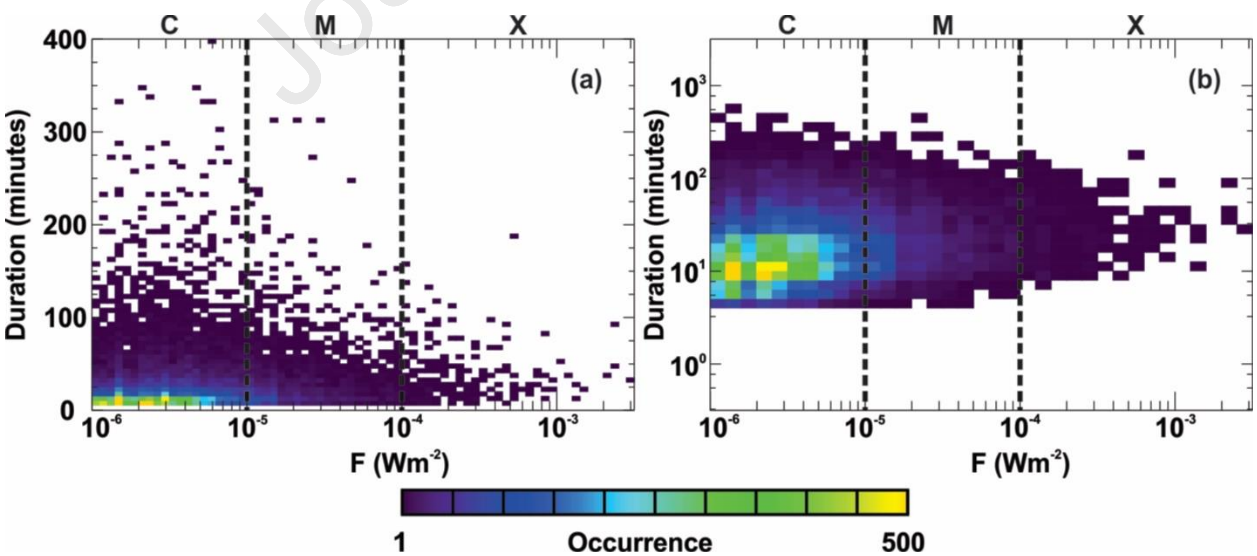

Figure 2: Occurrence density plots showing (a) duration and (b) the logarithm of duration of solar X-ray flares based on data reported versus the logarithm of the peak flare magnitude (F_{MAX}). Occurrence density is indicated by color according to the colour bar at the bottom of the Figure. Flare duration and F_{MAX} are based on data from the GOES X-ray sensor reports.

Table 2: Minimum, maximum, mean, and median duration of C, M, and X-class solar X-ray flares.

Classification	Number of Events	Minimum (minute)	Maximum (minute)	Median (minute)	Mean (minute)
All	25603	5	625	14	21
C	22049	5	625	13	20
M	3303	5	421	19	28
X	251	7	188	27	36
X1-X9	241	7	188	26	36
≥X10	10	12	93	36	39

To further examine trends between event duration and F_{MAX}, data presented in Figure 2b were binned in increments of 0.05 $\log_{10}(F_{MAX})$ Wm^{-2}, as shown in Figure 3. For each bin the distribution of the $\log_{10}$(Duration) observed in that bin was evaluated. The mean duration ($\overline{\mathrm{Duration}}$) and standard deviation (σ) of the distribution were determined provided the distribution was normal, evaluated using a Chi-square goodness of fit test with a significance level of α=0.1, and there were >10 points in the bin. Figure 3 is a log-log plot of $\overline{\mathrm{Duration}}$ versus F_{MAX}. The lower grouping of black filled circles represents $\overline{\mathrm{Duration}}$, and vertical lines at each point represent ±σ. Note that X-class and larger M-class X-ray flares are not included in Figure 3 as the data did not meet the criteria for determining $\overline{\mathrm{Duration}}$. The binned log-log data show excellent correlation between $\overline{\mathrm{Duration}}$ and F_{MAX}, as demonstrated by a Pearson correlation coefficient of R=0.98. The best-fit line to the data is

$$\log_{10}(\overline{\mathrm{Duration}}) = 0.16\log_{10}(F_{\mathrm{MAX}}) + 2.08\ (\mathrm{minutes}) \qquad (2a)$$

or equivalently

$$\overline{\mathrm{Duration}} = 118.85 F_{\mathrm{MAX}}{}^{0.16}\ (\mathrm{minutes}). \qquad (2b)$$

Based on this equation, the average durations for a C1, M1, M5, X1, X5, and X10 flares are 13, 18, 24, 27, 35, and 39 minutes, respectively, see Table 3. Variability demonstrated in the un-binned data set presented in Figure 2, combined with a need to define the worst-case scenario for operational robustness, suggests an upper limit in flare duration should be determined. The upper grouping of red filled circles indicates the 90th percentile of the normal distributions fit. The 90th percentile duration ($Duration_{90}$) also shows a clear relationship with F_{MAX}. The Pearson correlation coefficient is 0.95, and the best-fit line to the data is given by

$$\log_{10}(Duration_{90}) = 0.20\log_{10}(F_{MAX}) + 2.70\ (\mathrm{minutes}) \qquad (3a)$$

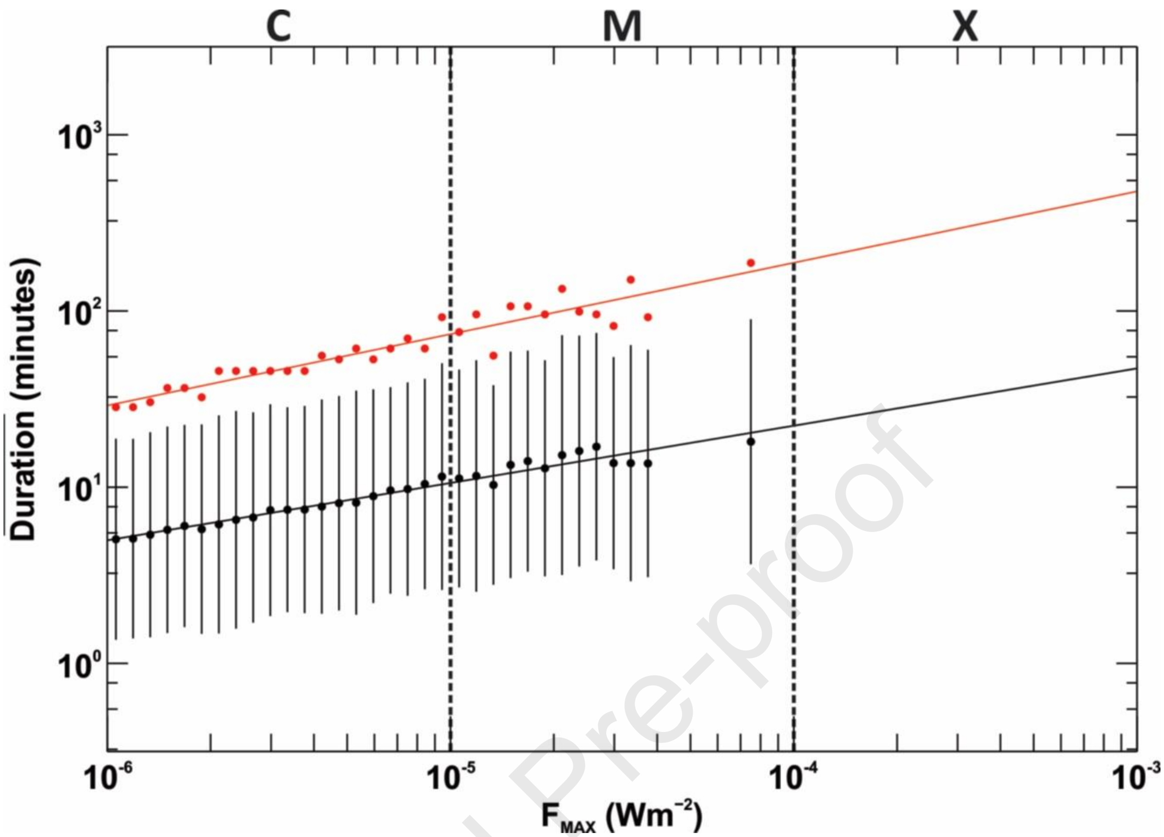

Figure 3: Log-log plot of event duration versus F_{MAX}. Data from Figure 2 have been binned in increments of *0.05* $\log_{10}(F_{MAX})$ Wm^{-2} to create normal distributions of $\log_{10}$(Duration) for each bin. Filled black circles and vertical lines represent the mean and standard deviation of the distributions. Solid black line is the best-fit line to the data. Upper filled red circles indicate the 90th percentile of the normal distributions, which are fit with the solid red line.

Table 3: Mean and 90th percentile of flare duration calculated from equations (2) and (3), respectively.

Classification	Duration (minutes)	
	Mean	90th percentile
C1	13	30
M1	18	48
M5	24	67
X1	27	77
X5	35	107
X10	39	123

or,

$$Duration_{90} = 498.08 {F_{MAX}}^{0.20} \text{ (minutes).} \tag{3b}$$

Based on this equation, the 90th percentile duration, which represents a reasonable maximum duration, ranges from 30 to 123 minutes for a C1 to X10 solar X-ray flare, as reported in Table 3.

The mean and 90th percentile fits described by equations (2) and (3) provide a general indication of the duration of a solar X-ray flare, characterized by solar X-ray flux, but there is significant variability in the data, as demonstrated by Figure 2, and a precise prediction of the event duration is not possible. A probabilistic model was developed to characterize the likelihood of an event having a specific duration based on the magnitude of the peak solar X-ray flux. The duration of the solar X-ray flare events presented in Figure 2, binned in increments of 0.05 $\log_{10}(F_{\mathrm{MAX}})$ Wm^{-2}, was evaluated to determine the probability of the event duration lasting 0-15, 15-30, 30-45, 45-60, 60-90, and >90 minutes, see Figure 4a. The probabilistic model shows a clear trend of decreasing probability of low duration events and an increasing probability of high duration events as the peak solar X-ray flux increases. For a C-class flare (10^{-6} Wm^{-2}) there is a roughly 40-60% probability the event duration will be < 15 minutes and an 80-90% probability the event duration will be < 30 minutes, which drops to ~30-40% and 60-80% for an M-class flare. The probability of a > 90 min flare is, on average, < 5% for a C or M class solar X-ray flare, which appears to increase for an X-class flare, although the statistics are low.

A duration model was created by fitting a 2nd order polynomial (quadratic) to the binned probability data. Figure 4b presents the quadratic fits to the data in Figure 4a, and the coefficients for the fit are provided in Table 4. Quantification of the relationships demonstrated in Figure 4a and 4b through this quadratic fit allows duration probability to be calculated for use in operational service development to characterize flare duration.

4.2 Duration of Shortwave Fadeout

Thus far, duration has been used to describe the temporal span of the solar X-ray flare based on start and end times defined in the GOES X-ray sensor reports referenced in Section 2. Perhaps more important to the development of an operational space weather service is the duration during which impacts are expected, which we will refer to as impact duration. Based on the threshold defined in Section 3, impact duration is the duration during which A_{30} is expected to exceed 0.5 dB. Impact duration was evaluated using 1-minute GOES solar X-ray flux data for 1986-2017, modelling A_{30} using equation (1) for specific fixed values of the SZA (chosen at 10° intervals), and locating periods where the modelled absorption exceeded 0.5 dB. Consecutive 1-minute intervals where the modelled absorption exceeded 0.5 dB were grouped into events, allowing a 5-minute gap of < 0.5 dB in an event, which effectively declusters closely spaced events. Data were binned in increments of 0.05 $\log_{10}(F_{\mathrm{MAX}})$ Wm^{-2}, and the probability of events ranging from 0 to >120 minutes duration was evaluated, and is presented in Figure 4c for SZA=0°.

For SZA=0°, 740 absorption events were identified, corresponding to 591 days during the 32-year period where one or more flares caused $A_{30} \geq 0.5$ dB. The distribution is not populated below an M4.1 solar X-ray flare as, according to equation (1), this corresponds to the minimum solar X-ray flux required for A_{30} to exceed 0.5 dB. As SZA increases, the number of events drops: 723, 689, 639, 571, 467, and 360 absorption events, and 583, 558, 522, 472, 393, and 314 days where one or more event was observed, were identified for SZAs of 10°, 20°, 30°, 40°, 50°, and 60°, respectively. Figure 4e shows the impact

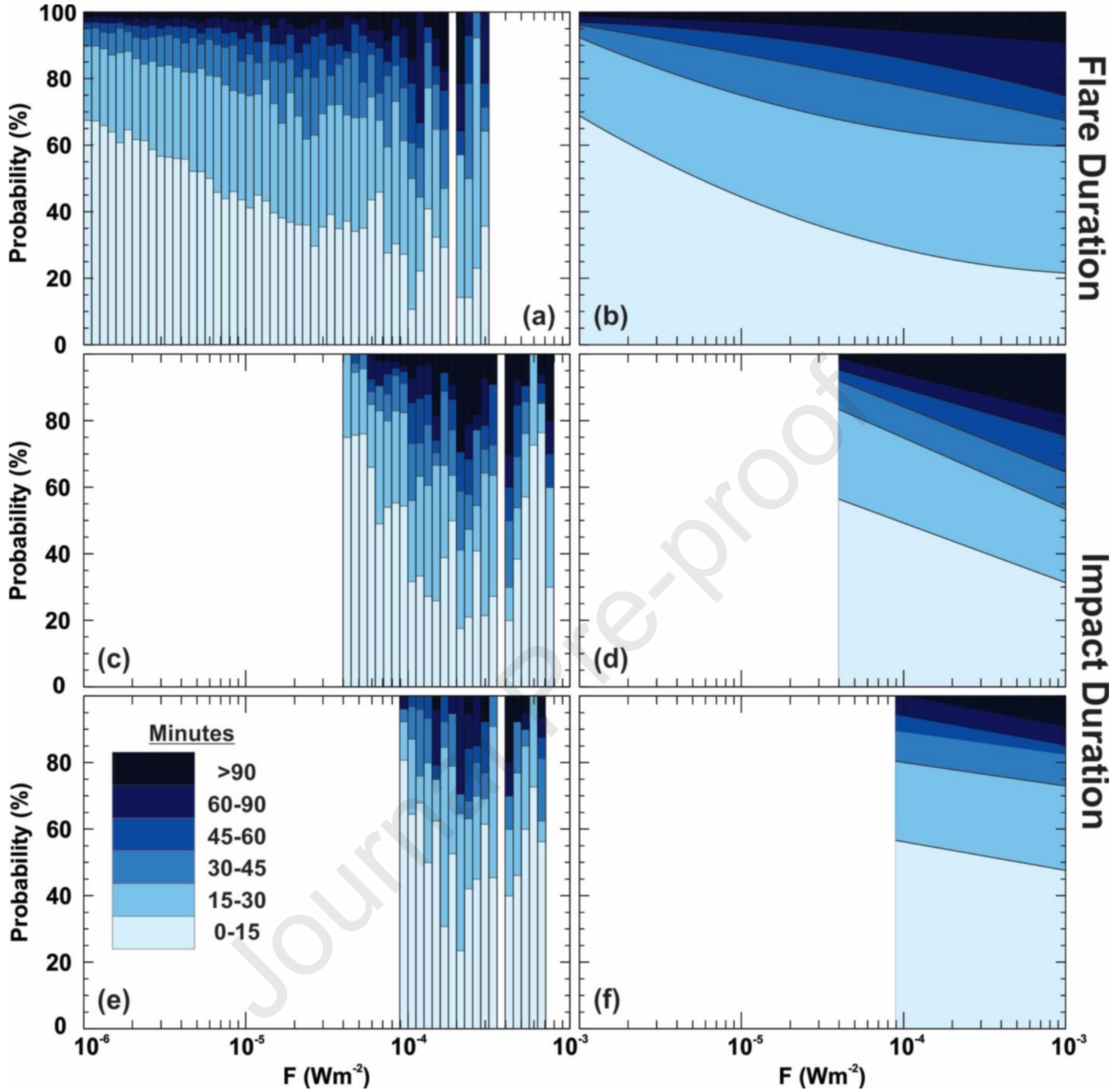

Figure 4: Probability of solar X-ray flare duration exceeding 0, 15, 30, 45, 60, and 90 minutes based on the magnitude of the peak solar X-ray flux during the flare. Duration in (a) and (b) is based on the flare start and end times recorded in the GOES X-ray sensor reports for 1997-2017. In (a) Solar X-ray flux is binned in increments of 0.05 $log_{10}(F_{MAX})$ Wm^{-2} for bins where there are >10 data points. (b) A quadratic fit to the probabilities in (a). In (c), (d), (e), and (f) duration represents impact duration which is the time during which $A_{30} \geq 0.5$ dB. Here absorption was calculated using equation (1) from 1-minute GOES 0.1-0.8 nm solar X-ray flux for 1986-2017 for (c) and (d) SZA = 0°, and for (e) and (f) SZA = 60°. In (d) and (f) the distributions in (c) and (e) were fit using a linear fit instead of a quadratic.

duration distribution for SZA=60°. Probability was not evaluated for SZA > 60° as the number of events (<250) dropped such that statistics could not be reliably determined for each duration interval. In general, as SZA increases the duration probability reduces as the overall absorption is smaller.

The impact duration distributions shown in Figures 4 c and e were modelled with a linear fit, and are shown in Figures 4 d and f, respectively. A quadratic fit was not used in these cases, as there was

Table 4: Solar X-ray flare duration is the quadratic fit to the probability bins illustrated in Figure 4b. Coefficients describe the equation probability = $C_0 + C_1*\log_{10}(F_{MAX}) + C_2*[\log_{10}(F_{MAX})]^2$. Duration of absorption > 0.5 dB (SZA dependence), or impact duration, is the linear fit to the probability bins for SZA of 0°, 10°, 20°, 30°, 40°, 50°, 60°, where examples at 0° and 60° are illustrated in Figures 4d and 4f, respectively. Coefficients describe the equation probability = $C_0 + C_1*\log_{10}(F)^2$.

	Number of Events	Duration (min)														
		0-15			15-30			30-45			45-60			60-90		
Solar X-ray Flare Duration																
		C_0	C_1	C_2	C_0	C_1	C_2	C_0	C_1	C_2	C_0	C_1	C_2	C_0	C_1	C_2
		52.6	23.4	4.3	85.3	18.2	3.2	31.3	-13.2	-0.4	18.6	-24.4	-1.9	73.8	-7.1	-0.5

Duration of Absorption > 0.5 dB (SZA dependence)	Number of Events	0-15		15-30		30-45		45-60		60-90	
		C_0	C_1	C_0	C_1	C_0	C_1	C_0	C_1	C_0	C_1
0°	740	-22.6	-18.0	-10.9	-21.4	5.6	-19.6	33.0	-14.1	45.8	-12.0
10°	723	-26.3	-19.0	-8.7	-21.1	5.8	-19.6	33.3	-14.1	48.2	-11.5
20°	689	-26.6	-19.3	1.4	-18.4	12.8	-18.0	40.6	-12.3	49.1	-11.2
30°	639	-28.4	-20.1	3.8	-17.9	28.2	-13.9	54.1	-9.0	57.9	-9.2
40°	571	3.3	-11.4	4.9	-17.8	43.4	-10.7	62.7	-7.1	60.8	-8.6
50°	467	-24.1	-19.8	21.5	-14.5	49.4	-9.7	62.0	-7.5	71.6	-6.6
60°	360	21.8	-8.6	51.6	-7.1	61.9	-6.8	58.6	-8.8	62.8	-9.3

insufficient data to constrain the fit. Compared to the duration of the solar X-ray flare shown in Figures 4 a and b, impact duration is shorter overall. For example, consider a solar X-ray flux of 10^{-4} (Wm^{-2}), which is the lower limit of an X-class flare. Based on the models shown in Figures 4 d and f, the impact duration has 50% and 56% probabilities of being < 15 minutes at SZA=0° and SZA=60°, respectively, whereas the flare duration has only a 28% probability of being < 15 minutes. Coefficients for the linear fits to the duration of absorption > 0.5 dB for SZA of 0° to 60° in 10° increments are provided in Table 4. The C_0 roughly increase with increasing SZA, with some deviation due to the drop in sample size for events observed at higher latitudes.

4.3 Spatial Distribution

Absorption (A_{30}) can be modelled from equation (1) for SZA spanning 0° (sub-solar point) to 90° (terminator) for C, M, and X-class solar X-ray flares, as presented in Figure 5a. A_{30} is plotted as a function of the logarithm of the 0.1 - 0.8 nm solar X-ray flux and SZA. White curves represent A_{30} of 0.1 dB, 0.5 dB, and 1.0 dB. Data above and to the left of each curve meet or exceed the curve threshold. For solar X-ray events approximately < M1 (1×10^{-5} Wm^{-2}) absorption is strictly < 0.1 dB. An X1 (1×10^{-4} Wm^{-2}) solar X-ray flare is expected to exceed A_{30} of 0.5 dB and 1.0 dB for SZA ≤ 65° and SZA ≤ 35°, respectively. As an example, an X1 flare is expected to cross the 0.5 dB thresholds indicating degradation of HF radio wave propagation for SZA as high as 65°. The 0.1 dB, 0.5 dB, and 1 dB absorption levels are crossed at increasingly higher SZA as solar X-ray flux increases; the 1 dB curve reaches ~85° for an X10 (1×10^{-3} Wm^{-2}).

At a given geographic coordinate, SZA varies as a function of time of day and day of year. Figure 5b shows the minimum daily SZA, where maximum photoionization is expected, for each day of the year with respect to geographic latitude. The white region near the equator indicates the shift of the sub-solar point, where SZA=0°, from the southern hemisphere at the December solstice to the northern hemisphere

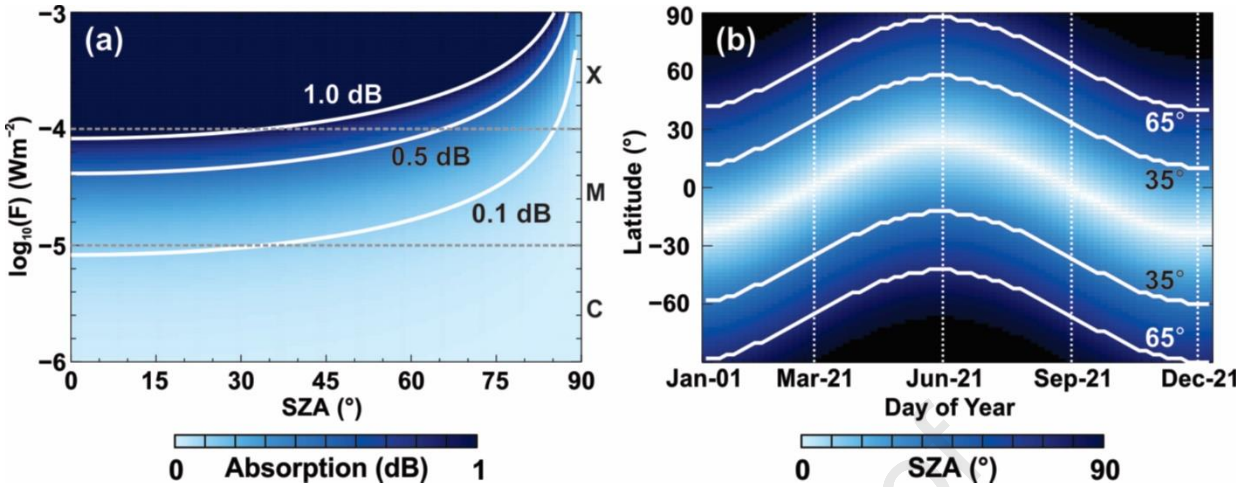

Figure 5: (a) Graphical representation of absorption at 30 MHz for a one-way vertical path, calculated from equation (1). Colour indicates magnitude of absorption calculated as a function of the logarithm of the 0.1-0.8 nm solar X-ray flux (F) and solar zenith angle (SZA). White curves represent 0.1 dB, 0.5 dB, and 1.0 dB absorption contours. (b) Minimum daily solar zenith angle calculated as a function of geographic latitude and day of year. Data are binned in increments of 5 days and 2°. White curves indicate SZA of 35° and 65° and represent the maximum high-latitude boundary for A_{30} of 1.0 dB and 0.5 dB expected for an X1 solar X-ray flare. Dotted vertical lines indicate solstice and equinox. Black shading during local winter indicates SZA > 90°.

at the June solstice. Near the winter solstice there are high-latitude regions where SZA is >90° and the local ionosphere does not experience overhead solar illumination and radio waves travelling through those regions are not expected to be impacted by shortwave fadeout. White curves indicate the 65° and 35° SZA contours in the Northern and Southern Hemispheres marking the high-latitude boundary for A_{30} of 0.5 dB and 1.0 dB, respectively, expected for an X1 solar X-ray flare. During local summer months an X1 solar X-ray flare can cause A_{30} of ≥ 0.5 dB at all latitudes, but during local winter months the maximum high-latitude extent is 40°-42° in either hemisphere.

Figure 6 shows A_{30} calculated from equation (1) for M5 and X1 solar X-ray flares at 12:00 UT for December solstice (upper panels), 21 March 2022 (middle panels), and June solstice (lower panels). The shift in the peak absorption from the southern hemisphere at the December solstice to the northern hemisphere at the June solstice is due to the tilt of the Earth, which is reflected in the cos(SZA) term in equation (1). For an M5 solar X-ray flare, A_{30} peaks at 0.6 dB and exceeds 0.5 dB between ±30° longitude for latitudes between -59° and 9° at December solstice, ±30° at equinox, and -9° and 59° at June solstice. Absorption for the X1 flare reaches a peak of 1.2 dB, and exceeds 0.5 dB within ~65° latitude and ~65° longitude of the subsolar point.

Equation (1) was evaluated to determine the minimum solar X-ray flux required to observe 0.5 dB and 1.0 dB absorption at different latitudes in the Northern Hemisphere. Each day of the year, the minimum SZA at latitudes spanning from 0° to 85° geographic latitude in 5° increments was evaluated and used to determine the minimum solar X-ray flux required to reach each threshold. Results are presented in Figure 7, where the lower and upper black curves indicate 0° and 85° latitudes, respectively, and darker black curves are for 0°, 20°, 40°, 60°, and 80°. Curves for geographic latitudes equatorward of ~10° reach a minimum at equinox and curves poleward of ~10° geographic latitude reach a minimum near the June solstice and maximize at the December solstice, consistent with the tilt of the Earth.

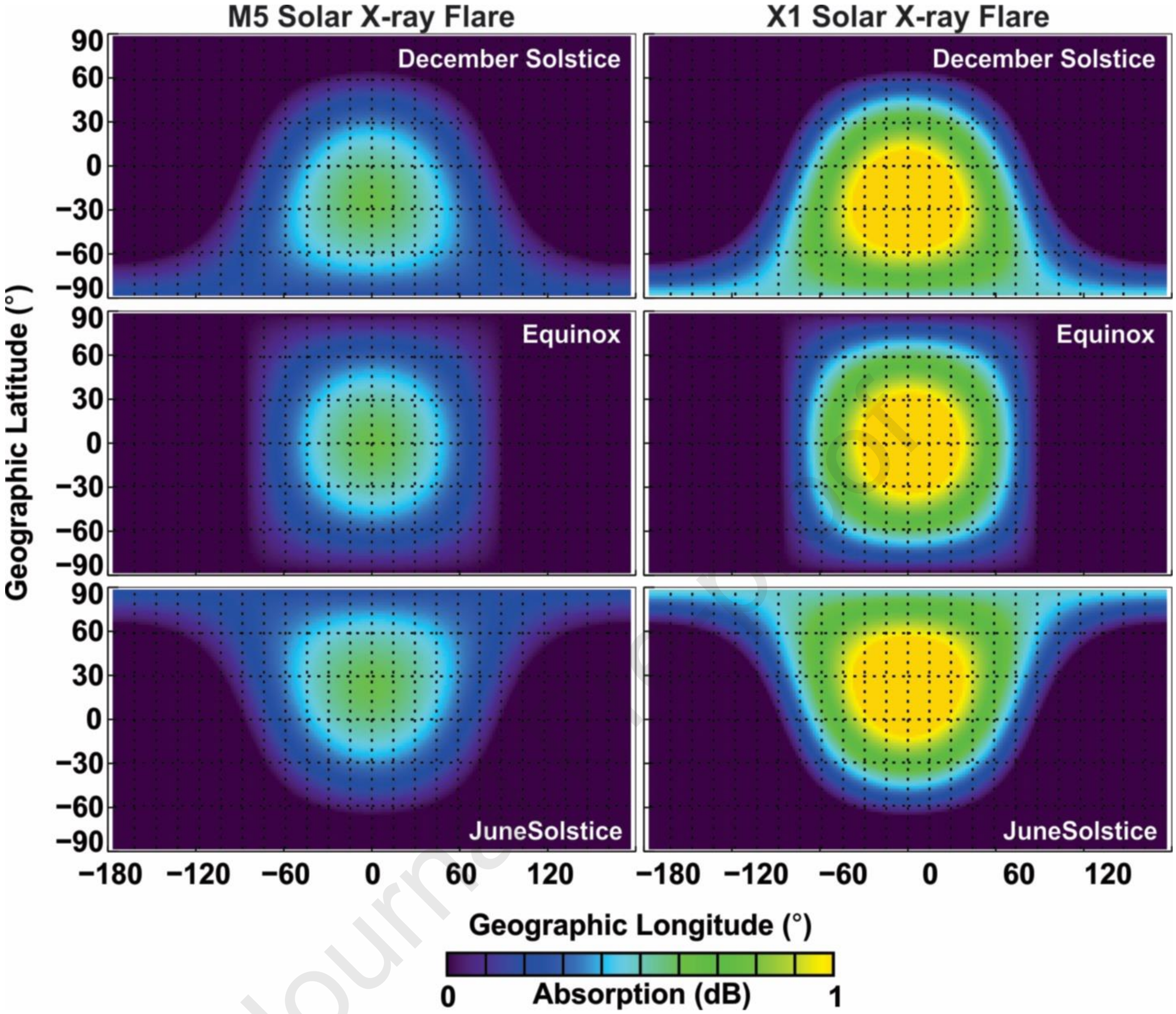

Figure 6: A_{30} due to an (left column) M5 and (right column) X1 solar X-ray flare as modelled from equation (1) at 12:00 UT for December solstice (upper panels), equinox (middle panels), and June solstice (lower panels). Horizontal lines indicate geographic latitude in 30° increments. Vertical lines indicate geographic longitude in 15° increments.

The minimum flux required to meet the 0.5 dB threshold is listed in Table 5 for SZA=[0°, 20°, 40°, 60°, 80°, and 90°]. The A_{30}=0.5 dB threshold is met for an M4.1 solar X-ray flare closer to the equator at ≤28° geographic latitude, representing equatorial geomagnetic latitudes. Closer to the high-latitude (geomagnetic) region, solar X-ray flares must only reach M5.2 and X7.5 to cross the 0.5 dB threshold for 60° and 80° geographic latitude, respectively. The minimum solar x-ray class at which A_{30} exceeds 1.0 dB ranges from M8.3 at 20° geographic latitude to X1.5 at 80° geographic latitude. The minimum flux required to exceed 0.5 dB and 1.0 dB at the northernmost geographic latitude of 90° is X1.0 and X2.0, respectively.

Figure 8 shows the distribution of solar X-ray flares reported in the GOES X-ray sensor reports for 1997-2017 binned in increments of 0.05 $\log_{10}(F_{MAX})$ Wm^{-2}. Dashed and solid vertical lines indicate the minimum solar X-ray class required for A_{30} to exceed 0.5 dB and 1.0 dB at geographic latitudes of 0° and 90°, respectively. Table 5 includes the number of occurrences where these thresholds were crossed which

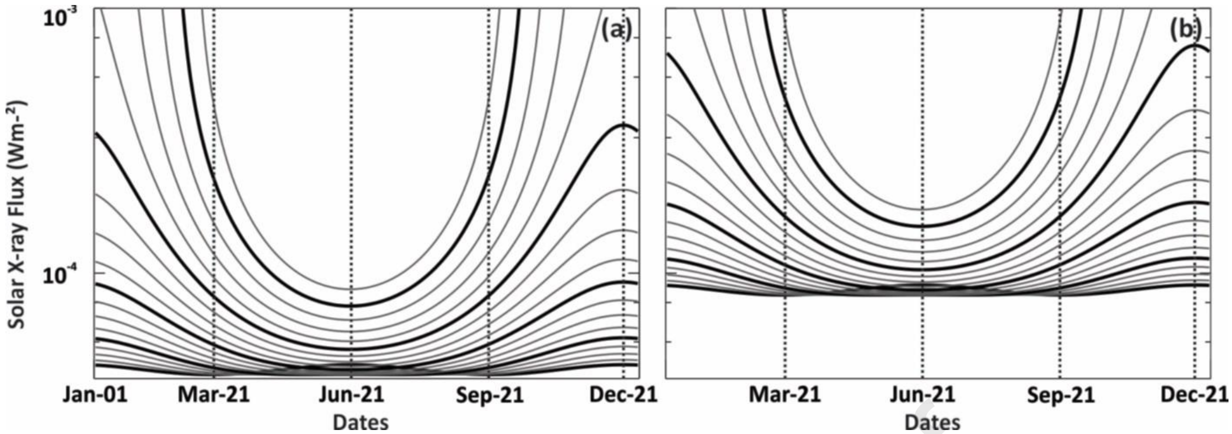

Figure 7: Minimum solar X-ray flux required to exceed A_{30} of (a) 0.5 dB and (b) 1.0 dB each day of the year in 2022. Curves represent minimum solar X-ray flux calculated using equation (1) at latitudes ranging from 0° to 85° geographic latitude in 5° increments. Dark curves are overplotted in 20° increments. Minimum solar X-ray flux for each of the dark curves is reported in Table 5. Dotted vertical lines indicate solstice and equinox.

Table 5: Minimum solar X-ray flare size required for A_{30} to cross the 0.5 dB and 1.0 dB at geographic latitude of 0°, 20°, 40°, 60°, and 80° geographic latitudes, and number of occurrences of events exceeding the solar X-ray flare size threshold in 1997-2017.

Geographic Latitude (°)	X-ray Flare Size		Occurrence ≥ X-ray Flare Size	
	0.5 dB	1.0 dB	0.5 dB	1.0 dB
0°	M4.1	M8.3	699	318
20°	M4.1	M8.3	699	318
40°	M4.3	M8.6	648	305
60°	M5.2	X1.0	532	251
80°	M7.5	X1.5	372	154
90°	X1.0	X2.0	251	109

ranges from 699 occurrences of solar X-ray flares ≥ M4.1 to 109 occurrences of solar X-ray flares ≥ X2.0. An M4.1 solar X-ray flare marks the 97.3rd percentile of the data; these events are non-uniformly distributed with more events occurring during periods of solar maximum than solar minimum.

5. Discussion and conclusions

This paper examines the risk of shortwave fadeout to high frequency (HF) radio wave propagation by evaluating the duration of enhanced solar X-ray flux, the duration where impacts are expected for HF systems, and the spatial extent of expected impacts.

To assess risk, a threshold in the absorption expected at 30 MHz for a one-way vertical path (A_{30}) was established to indicate when signal degradation is likely. By closely examining riometer and SuperDARN data for an X2.1 solar X-ray flare, a threshold of A_{30}=0.5 dB was selected. The relevance of this threshold was demonstrated for a polar cap absorption event observed February - March 2014 by an HF transmission network operating in Canada. An impact-based risk threshold, such as absorption, as opposed to a driver-based risk threshold, such as magnitude of the solar X-ray flux, is a valuable tool for

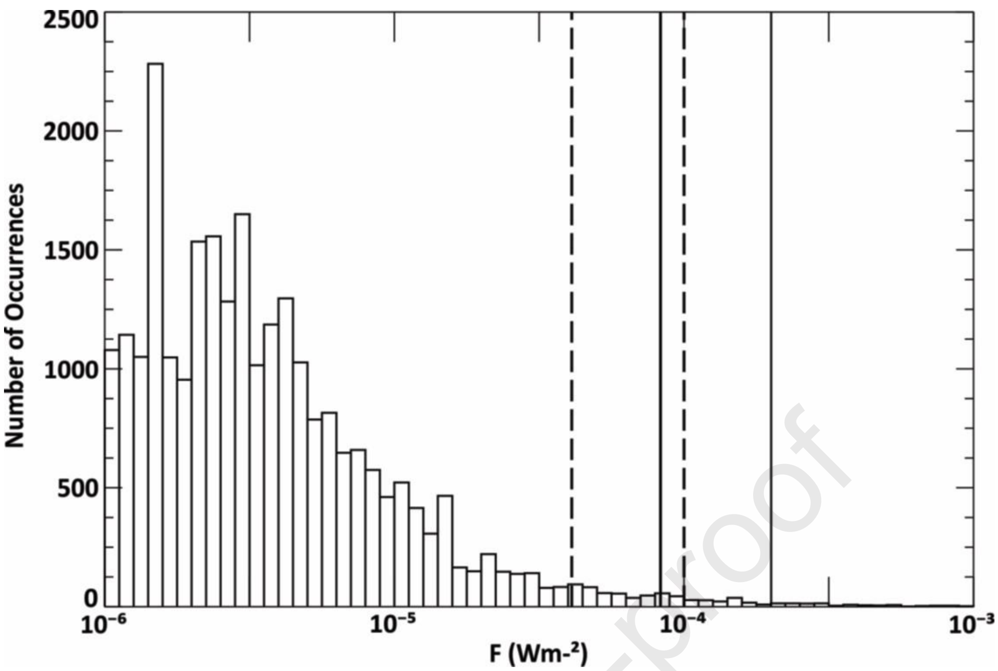

Figure 8: Distribution of the logarithm of the peak flare magnitude (F_{MAX}) for ≥ C-class solar X-ray flares observed 1997-2017 based on data from the GOES X-ray sensor reports. Data are binned in increments of 0.05 $log_{10}(F_{MAX})$ Wm^{-2}. Dashed and solid vertical lines indicate the minimum solar X-ray flux for A_{30} of 0.5 dB and 1.0 dB, respectively, associated with a geographic latitude of 0° and 90°, as indicated in Table 5.

characterizing threats to HF radio wave propagation, especially when evaluating the overall threat from multiple sources.

Solar X-ray flare data from GOES X-ray sensor reports for 1997-2017 were used to calculate event duration for all ≥ C class non-overlapping events. Mean event duration ($\overline{\mathrm{Duration}}$) and 90th percentile duration (*Duration₉₀*) were related to the magnitude of the peak solar X-ray flux (F_{MAX}) in the 0.1-0.8 nm waveband through:

$$\overline{\mathrm{Duration}} = 118.85 F_{\mathrm{MAX}}{}^{0.16}\ \text{(minutes), and}$$
$$\mathrm{Duration}_{90} = 498.08 F_{\mathrm{MAX}}{}^{0.20}\ \text{(minutes),}$$

respectively. These equations correspond to mean durations of 13, 18, 24, 27, 35, and 39 minutes and 90th percentile durations of 30, 48, 67, 77, 107, and 123 minutes for solar X-ray flares of magnitude C1, M1, M5, X1, X5, and X10, respectively. These results are consistent with those obtained by Xiong et al. (2021), who examined solar flares in solar cycles 22, 23, and 24, and Joshi et al. (2010), who examined solar flares in solar cycles 21, 22, and 23. For example, Xiong et al. (2021) reported duration means of 29-52 minutes for M-class flares and 35-98 minutes for X-class flares and 90th percentile values of 56-107 minutes and 78-202 minutes for M and X-class flares, respectively.

Distributions in the paper by Tao et al. (2020) for 120 radio blackouts for ≥ C1 events observed in ionosonde data show duration range of roughly 15-90 minutes. Nogueira et al. (2015) report a 70-minute blackout for an equatorial ionosonde for an X2.8 solar X-ray flare. Considering that the Tao et al. (2020) and Nogueira et al. (2015) results represent impact duration opposed to flare duration, the slightly reduced range of duration is consistent with results presented here. Sripathi et al. (2013) reports a more conservative 30-minute blackout in ionosonde data for an X7 flare on 09 August 2011 for an equatorial station located with a SZA of 17°. The reduced duration is possibly a function of the 10-minute sampling resolution of the ionosonde.

Probabilistic duration models were determined to describe both the duration of solar X-ray flare events, and the duration of the expected impact to HF systems. Both event duration and impact duration showed a trend of increasing length with increasing magnitude of the peak solar X-ray flux, in agreement with numerous studies (Temmer et al., 2001; Veronig et al., 2002; Joshi et al., 2010; Tao et al., 2020; Xiong et al., 2021). The probability of flare duration and impact durations of 0-15, 15-30, 30-45, 45-60, 60-90, and >90 minutes are presented in Figure 4 and Table 4. For example, an X1 flare has a 27.8% probability of being < 15 min, a 63.7% probability of being <30 min and a 14.2% probability of being > 60 min. The corresponding impact durations probabilities at SZA=0° are 49.4%, 74.7%, 10.6% for < 15 min, < 30 min, and > 60 min, respectively. At SZA=60° probabilities change to 56.2% for < 15 min, 80.0% for < 30 min, and 6.2% for >60 min. As SZA increases from 0° to 180° the likelihood of a low duration event increases, which is accounted for in the cos(SZA) dependence in equation (1). This feature is also reported by Chakraborty et al. (2018) who observed decreasing duration of ionospheric impact with increasing SZA, as characterized by SuperDARN for flares simultaneously observed by multiple stations radars. Based on a study of 8 M and X-class solar X-ray flares using data from low and mid-latitude ionosonde stations for varying SZA, Barta et al. (2019) also reported largest impact duration for smaller SZA.

Tao et al. (2020) also used the GOES solar X-ray reports to characterize impact duration based on an analysis of 36 years of ionosonde data for the Kokubunji, Tokyo, Japan station (35.71°N, 138.49°E) which pulses vertically across 1-30 MHz. The evaluation was focused on 05-19 LT (20-10 UT), when the ionosonde was located on the dayside. When impact is defined as radio blackout in the ionosonde data, Tao et al. (2020) observed that for solar X-ray flares ≥ C1, impact duration was <30 minutes for 78-79% of events, 60 - 105 minutes for 11-14% of events, and >120 minutes for 2.5-4.2% of events. This agrees with the probability distributions in Figures 4c which observe <30 minutes for 73% of events, 60-105 minutes for 7% of events, and >120 minutes for 5% of events for impact duration considered at SZA=0°. At SZA=60° the corresponding values are 74%, 9%, and 4%. Discrepancies with Tao et al. (2020) are explained by the 15-minute resolution of the ionosonde data compared to the 1-minute resolution solar X-ray flux used to evaluate impact duration in this study, and the fact that SZA ranges from ~10° to 120° between 05 and 09 LT at the location of the ionosonde station, opposed to the SZA=0° and SZA=60° results reported here.

Solar X-ray flares are often considered to be a low-latitude phenomenon as their SZA dependence indicates maximum impact at the Earth's subsolar point. To demonstrate the spread of expected impacts, the spatial distribution of the A_{30} shortwave fadeout model was thoroughly explained by graphically demonstrating the SZA dependence for varying levels of solar X-ray flux and relating this to geographic latitude and longitude. As an example, for an X1 solar X-ray flare, the 0.5 dB threshold is expected to be crossed for SZAs as high as 65°, and for an X10 solar X-ray flare 1.0 dB can be exceeded across the sunlit side of the Earth reaching to SZAs of 90°.

The model was also evaluated to determine the minimum solar X-ray flare required to exceed 0.5 dB. For latitudes of 0°, 20°, 40°, 60°, and 80° the minimum solar X-ray flares, observed during the June solstice, were M4.1, M4.1, M4.3, M5.2, and M7.5. By comparing these thresholds with flares listed in the GOES X-ray sensor reports, it was found that these numbers represent only the upper 97.3rd percentile of the data, and are non-uniformly distributed, with more events occurring during periods of solar maximum than solar minimum.

A thorough understanding of both the duration of the driving phenomenon and the impact duration of shortwave fadeout, and the spatial extent of the impact contribute to the development of space weather services that reduce risk to sensitive systems that rely on HF radio wave propagation.

Acknowledgements

This work was supported by the Natural Resources Canada Lands and Minerals Sector, Canadian Hazards Information Service. GOES solar X-ray flux data are available from the National Geophysical Data Centre (NGDC) (http://www.ngdc.noaa.gov/stp/satellite/goes/dataaccess.html). NRCan riometer data may be obtained from http://www.spaceweather.gc.ca. The authors acknowledge the use of SuperDARN data. SuperDARN is a collection of radars funded by national scientific funding agencies of Australia, Canada, China, France, Italy, Japan, Norway, South Africa, United Kingdom and the United States of America. SuperDARN data are available from the SuperDARN website hosted by Virginia Tech (http://vt.superdarn.org). The authors thank Dr. Taylor Cameron for helpful discussions. This is NRCan publication 20220387.

References

Barta, V., Gabriella, S. Berényi, K. A., Kis, Á; Williams, E., 2019. Effects of solar flares on the ionosphere as shown by the dynamics of ionograms recorded in Europe and South Africa, Ann. Geophys., 37, pp. 747-761, https://doi.org/10.5194/angeo-37-747-2019.

Belrose, J. S., Cetiner, E., 1962. Measurement of electron densities in the ionospheric D-region at the time of a 2+ solar flare, Nature, 196, pp. 688-690.

Berngardt , O. I., Ruohoniemi, J. M., Nishitani, N, Shepherd, S. G., Bristow, W. A., Miller, E. S., 2018. Attenuation of decameter wavelength sky noise during x-ray solar flares in 2013-2017 based on the observations of midlatitude radars, Journal of Atmospheric and Solar-Terrestrial Physics, 173, 1-13, https://doi.org/10.1016/j.jastp.2018.03.022.

Boteler, D. H. 2018. “Chapter 26 - Dealing with Space Weather: The Canadian Experience”. In Natalia Buzulukova (Ed.), Extreme Events in Geospace, pp 635-656. https://doi.org/10.1016/B978-0-12-812700-1.00026-1.

Browne, S., Hargreaves, J. K., and Honary, B., 1995. An imaging riometer for ionospheric studies, Electronics & Communications Engineering Journal, 7 (5), 209-217, https://doi.org/10.1049/ecej:19950505.

Cameron, T. G., Fiori, R. A. D., Warrington, E. M., Stocker, A. J., Thayaparan, T., Danskin, D. W., 2021. Characterization of high latitude radio wave propagation over Canada, Journal of Atmospheric and Solar-Terrestrial Physics, 2021, 105666, ISSN 1364-6826, https://doi.org/10.1016/j.jastp.2021.105666.

Cannon, P., Angling, M., Barclay, L., Curry, C., Dyer, C., Edwards, R., Greene, G., Hapgood, M., Horne, R., Jackson, D., Mitchell, C., Owen, J., Richards, A., Rogers, C., Ryden, K., Saunders, S., Sweeting, M., Tanner, R., Thomson, A., Underwood, C., 2013. Extreme space weather: impacts on engineered systems and infrastructure. London, Royal Academy of Engineering.

Chakraborty, S., Ruohoniemi, J. M., Baker, J. B. H., Nishitani, N., 2018. Characterization of short-wave fadeout seen in daytime SuperDARN ground scatter observations, Radio Science, 53 (4), 472-484, https://doi.org/10.1002/2017RS006488.

Chakraborty, S., Baker, J. B. H., Ruohoniemi, J. M., Kunduri, B. S. R., Nishitani, N., Shepherd, S. G., 2019. A study of SuperDARN response to co-occurring space weather phenomena, Space Weather, 17, 1351–1363. https://doi.org/10.1029/2019SW002179.

Chakraborty, S. J., Baker, B. H., Fiori, R. A. D., Zawdie, K. A., Ruohoniemi, J. M., 2021. A modeling framework for estimating ionospheric HF absorption produced by solar flares, *Radio Science,* 56(10), https://doi.org/10.1029/2021RS007285.

Chisham, G., Lester, M., Milan, S. E., Freeman, M. P., Bristow, W. A., Grocott, A., et al., 2007. A decade of the Super Dual Auroral Radar Network (SuperDARN): scientific achievements, new techniques and future directions, *Surveys in Geophys*ics, 28, 33–109, https://doi.org/10.1007/s10712-007-9017-8.

Cliver, E. (2001). Solar flare classification In P. Murdin (Ed.), Encyclopedia of Astronomy and Astrophysics. Bristol: Institute of Physics Publishing. https://doi.org/10.1888/0333750888/2285.

Danskin, D. W., Boteler, D., Donovan, E., and Spanswick, E., 2008. The Canadian riometer array, Proc. of the 12th International Ionospheric Effects Symposium, IES 2008.

Davies, K, 1990. Ionospheric Radio, IEE Electromagn. Ser. Peter Peregrinus, London, vol. 31.

Eccles, J. V., Hunsucker, R. D., Rice, D, Sojka, J. J. (2005). Space weather effects on mid-latitude HF propagation paths: Observations and a data-driven D-region model, Space Weather, 3(1), https://doi.org/10.1029/2004SW000094.

Fiori, R. A. D., Koustov, A. V., Chakraborty, S., Ruohoniemi, J. M., Danskin, D. W., Boteler, D. H., ad Shepherd, S. G., 2018. Examining the Potential of the Super Dual Auroral Radar Network for Monitoring the Space Weather Impact of Solar X-Ray Flares. Space Weather, 16, 1348–1362, https://doi.org/10.1029/2018SW001905.

Fiori, R. A. D., Chakraborty, S., Nikitina, L., 2022a, Data-based optimization of a simple shortwave fadeout absorption model, Journal of Atmospheric and Solar-Terrestrial Physics, https://doi.org/10.1016/j.jastp.2022.105843.

Fiori, R. A. D., Kumar, V., Boteler, D. H., Terkildsen, M. B., 2022b. Occurrence of moderate to severe level space weather conditions likely to impact high frequency radio wave propagation used by aviation, Journal of Space Weather and Space Climate, 12, https://doi.org/10.1051/swsc/2022017.

Frissell, N. A., Miller, E. S., Kaeppler, S. R., Ceglia, F., Pascoe, D., Sinanis, N., Smith, P., Williams, R., Shovkoplyas, A., 2014. Ionospheric sounding using real-time amateur radio reporting networks, Space Weather, 12, 651-656, https://doi.org/10.1002/2014SW001132.

Frissell, N. A., Vega, J. S., Markowitz E., Gerrard, A. J., Engelke, W. D., Erickson, P. J., Miller, E. S., Luetzelschwab R. C., Bortnik, J., 2019. High-frequency communications response to solar activity in September 2017 as observed by amateur radio networks, Space Weather, 17(1), 118-132, https://doi.org/10.1029/2018SW002008.

Greenwald, R. A., Baker, K. B., Dudeney, J. R., Pinnock, M., Jones, T. B., Thomas, E. C., Villain, J.-P., Cerisier, J.-C., Senior, C., Hanuise, C., Hunsuker, R. D., Sofko, G., Koehler, J., Nielsen, E., Pellinen, R., Walker, A. D. M., Sato, N., & Yamagishi, H. (1995), DARN/SuperDARN: A global view of the dynamics of high-latitude convection, *Space Science Reviews*, 71, 763–796, https://doi.org/10.1007/BF00751350.

Hapgood, M., Angling, M. J., Attrill, G., Bisi, M., Cannon, P. S., Dyer, C., Eastwood, J. P., Elvidge, S., Gibbs, M., Harrison, R. A., Hord, C., Horne, R. B., Jackson, D. R., Jones, B., Machin, S., Mitchell, C. N., Preston, J., Rees, J., Rogers, N. C., Routledge, G., Ryden, K., Tanner, R., Thomson, A. W. P., Wild, J. A., Willis, B., 2021. Development of Space Weather Reasonable Worst-Case Scenarios for the UK National Risk Assessment, Space Weather, 19(4), https://doi.org/10.1029/2020SW002593.

Hosokawa K., Iyemori, T., Yukimatu, A. S., Sato, N., 2000. Characteristics of solar flare effect in the high-latitude ionosphere as observed by the SuperDARN radars, Advances in Polar Upper Atmospheric Research, 14, 66-75.

ICAO (2010), HF Frequency Management Guidance Materiel for the South Pacific Region, Version 1.0, https://www.icao.int/APAC/documents/edocs/cns/HF_radio_GM%20_ISPACG_Ver1.pdf (last accessed 05 October 2022).

ICAO (2018), Annex 3 to the Convention on International Civil Aviation, Meteorological Service for International Air Navigation, ICAO International Standards and Recommended Practices, Twentieth Edition, July 2018, http://store.icao.int/products/annex-3-meteorological-service-for-international-air-navigation (last accessed 05 October 2022).

ICAO (2019), Manual on Space Weather Information in Support of International Air Navigation, ICAO Doc 10100, First Edition, https://store.icao.int/products/manual-on-space-weather-information-in-support-of-international-air-navigation-doc-10100 (last accessed 05 October 2022).

Joshi, N.C., Bankoti, N.S., Pande, S., Pande, B., Uddin, W., Pandey, K., 2010. Statistical analysis of soft X-ray solar flares during solar cycles 21, 22 and 23. New Astron. **15**(6), 538–546, https://doi.org/10.1016/j.newast.2010.01.002.

Kikuchi, T., Sugiuchi, H., Ishimine, T., Maeno, H., Honma, S., 1986. Solar-terrestrial disturbances of June-September 1982. IV. Ionospheric disturbances. 1. HF Doppler observations, Journal of the Radio Research Laboratories, 33(1), 239-255.

Knipp, D. J., Bernstein, V., Wahl, K., and Hayakawa, H., 2021. Timelines as a tool for learning about space weather storms, J. Space Weather Space Clim, 11 (29), https://doi.org/10.1051/swsc/2021011.

Lam, H.-L., 2011. From early exploration to space weather forecasts: Canada's geomagnetic odyssey. Space Weather, 9, https://doi.org/10.1029/2011SW000664.

Levine, E. V., Sultan, P. J., Teig, L. J., 2019. A parameterized model of X-ray solar flare effects on the lower ionosphere and HF propagation, *Radio Science, 54,* p. 168–180, https://doi.org/10.1029/2018RS006666.

Machol, J., Viereck, R., 2016. GOES X-ray Sensor (XRS) Measurements. https://ngdc.noaa.gov/stp/satellite/goes/doc/GOES_XRS_readme.pdf (last accessed 05 October 2022).

Mitra, A., 1974. Ionospheric effects of solar flare, vol. 46, Astrophysics and space science library. Massachusetts: Reading. https://doi.org/10.1007/978-94-010-2231-6.

Nishitani, N., Ruohoniemi, J.M., Lester, M. et al., 2019. Review of the accomplishments of mid-latitude Super Dual Auroral Radar Network (SuperDARN) HF radars. Prog Earth Planet Sci 6, 27. https://doi.org/10.1186/s40645-019-0270-5

Nogueira, P. A. B., Souza, J. R., Abdu, M. A., Paes, R. R., Sousasantos, J., Marques, M. S., Bailey, G. J., Denardini, C. M., Batista, E. S., Takahashi, H., Cueva, R. Y. C., and Chen, S. S., 2015. Modeling the equatorial and low-latitude ionospheric response to an intense X-class solar flare, J. Geophys. Res., 120, pp. 3021-3032, https://doi.org/10.1002/2014JA020823.

NORSTAR, 2014. CANOPUS Quiet Day Curve Generation. Available online: http://aurora.phys.ucalgary.ca/norstar/rio/doc/CANOPUS_Riometer_Baselining.pdf (accessed 24 May 2023).

de Paula, V., Segarra, A., Altadill, D., Curto, J. J., and Blanch, E., 2022), Detection of solar flares from the analysis of signal-to-noise ratio recorded by digisonde at mid-latitudes, Remote Sensing, 14(8), https://doi.org/10.3390/rs14081898.

Reep J. W., Knizhnik, K. J., 2019. What determines the X-ray intensity and duration of a solar flare, The Astrophysical Journal, 874(2), https://doi.org/https://doi.org/10.3847/1538-4357/ab0ae7.

Schumer, E. A., 2009. Improved modeling of midlatitude D-region ionospheric absorption of high frequency radio signals during solar X-ray flares, PhD Dissertation, AFIT/DS/ENP/09-J01, U.S. Air Force, Wright-Patterson Air Force Base, Ohio.

Sripathi, S., Balachandran, N., Veenadhari, B., Singh, R., and Emperumal, K., 2013. Response of the equatorial and low-latitude ionosphere to an intense X-class solar flare (X7/2B) as observed on 09 August 2011, J. Geophys. Res., 118, pp. 2648-2659, https://doi.org/10.1002/jgra.50267.

Swalwell, B., Dalla, S., Kahler, S., White, S. M., Ling, A., Viereck, R., Veronig, A., 2018. The reported durations of GOES soft X-ray flares in different solar cycles, Space Weather, 16(6), https://doi.org/10.1029/2018SW001886.

Tao, C., Nishioka, M., Saito, S., Shiota, D., Watanabe, K., Nishizuka, N., Tsugawa, T., and Ishii, M., 2020. Statistical analysis of short-wave fadeout for extrememem space weather event estimation, Earth, Planets and Space, 72 (173), https://doi.org/10.1186/s40623-020-01278-z.

Temmer, M., Veronig, A., Hanslmeier, A., Otruba, W., Messerotti, M., 2001. Statistical analysis of solar Hα flares, Astronomy & Astrophysics, 375, pp. 1049-1061, https://doi.org/10.1051/0004-6361:20010908.

Thayaparan, T., Villeneuve, H., Warrington, M., Themens, D., Cameron, T., Fiori, R., 2022. Real-time frequency management system (FMS) for Sky-Wave High-Latitude Over-the-Horizon radar (OTHR), International Radar Symposium 2022 (IRS-2022), conference paper, https://doi.org/10.1109/TGRS.2022.3193015.

Watanabe, K., Nishitani, N., 2013. Study of ionospheric disturbances during solar flare events using the SuperDARN Hokkaido radar, Advances in Polar Science, 24 (1), 12-18, https://doi.org/10.3724/SP.J.1085.2013.00012.

Veronig, A., Temmer, M., Hanslmeier, A., Otruba, W., Messerotti, M., 2002. Temporal aspects and frequency distributions of solar soft X-ray flares. Astron. Astrophys. **382**(3), 1070–1080, https://doi.org/10.1051/0004-6361:20011694.

Xiong, B., Wang, T., Li, X., Yin, Y., 2021. Statistical analysis of soft X-ray solar flares during solar cycles 22, 23, and 24, Astrophysics and Space Science, 366(1), https://doi.org/10.1007/s10509-020-03909-z.

Declaration of interests

☒ The authors declare that they have no known competing financial interests or personal relationships that could have appeared to influence the work reported in this paper.

☐ The authors declare the following financial interests/personal relationships which may be considered as potential competing interests: